Turning depths: Evanescent to propagating wave kinetic energy density

Allison Lee and Julie Crockett

Phys. Rev. Fluids **4**, 034803 — Published 14 March 2019

DOI: 10.1103/PhysRevFluids.4.034803

Turning depths: evanescent to propagating wave kinetic energy density

Allison Lee and Julie Crockett*

Brigham Young University

(Dated: February 22, 2019)

Abstract

Tidal flow over oceanic topography generates internal waves when the natural frequency (N) of the water is greater than the tidal frequency (ω). When $N < \omega$, evanescent waves are generated. Although the amplitude and kinetic energy of evanescent waves decay rapidly, if the wave reaches a turning depth, where $N = \omega$, and moves into a region where $N > \omega$, the evanescent wave becomes an internal wave. This work expands upon previous research of varying stratifications by investigating the kinetic energy density in internal waves generated by evanescent waves passing through a turning depth. An analytical model is presented and compared to synthetic schlieren experiments of two Gaussian shaped topographies. The model and experiments both indicate that the kinetic energy density of internal waves increases with decreasing topographic slope, when the distance between the topography and the turning depth decreases, and when the average Froude number in the evanescent region is close to one. The model is used to estimate the normalized kinetic energy density of internal waves generated from an oceanic feature located within an evanescent region.

* crockettj@byu.edu

I. INTRODUCTION

Internal waves are uniquely formed in stratified fluids such as the atmosphere and ocean. The strength of the stratification is proportional to the variation in density in a fluid and is defined by the natural frequency of unforced oscillations, N which is defined as

$$N^2 = \frac{-g}{\rho_0}\frac{d\rho}{dz} \tag{1}$$

where g is the gravitational constant, ρ_0 is a reference density, and $d\rho/dz$ is the change in density with respect to height. One well known generator of internal waves in the ocean is tidal flow over oceanic bathymetry, specifically the M2 semidiurnal tide, with a frequency $\omega_{M2} = 1.4052 \times 10^{-4}\ s^{-1}$ [1]. The kinetic energy of internal waves generated from oceanic topography depends on many factors, including the strength of the stratification and the shape of the topography. The strength of the stratification defines whether internal waves or evanescent waves will be formed. Internal waves are formed when N is greater than the excitation frequency (ω) and they suffer little to no viscous dissipation as they propagate. Figure 1a depicts an internal wave generated by tidal motion across an idealized oceanic topography. Evanescent waves form in the opposite scenario, where $N < \omega$ as depicted in Fig. 1b. An evanescent wave has no vertical structure as a propagating wave does and as it transmits energy vertically the amplitude decays at an exponential rate [2]. King et al. [1] used data from the World Ocean Circulation Experiment (WOCE) to estimate variations in N across the oceans in order to locate evanescent regions and turning depths, or locations where the natural frequency is equal to the forced wave frequency associated with ω_{M2}. They found that these turning depths occur frequently in deep oceans where east-west tides dominate. If an evanescent wave reaches a turning depth, it becomes a propagating internal wave, as shown in Fig. 1c where the evanescent wave reaches the turning depth (dashed line) and then forms a propagating internal wave [2]. While internal waves are known to have significant energy and are widely studied, evanescent waves are not often considered to have an impact on the ocean due to the rapid decay rate of the amplitude and energy content. However, if a significant portion of the original evanescent wave energy reaches a propagating region, the internal waves formed may have an important impact on the ocean energy budget.

Significant research has been accomplished in both varying stratifications and internal waves approaching evanescent regions. Pedlosky [3] used linear theory and the WKB ap-

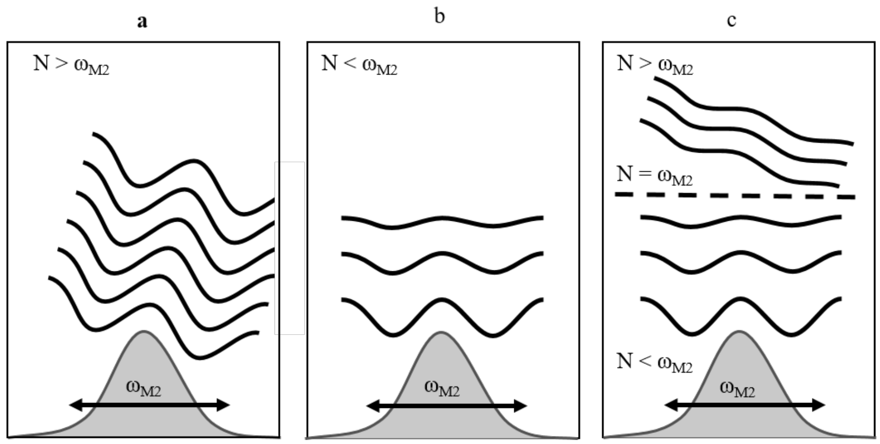

FIG. 1. A propagating internal wave is shown in (a) and the vertically decaying evanescent wave is seen in (b). In (c), the a turning depth indicates the boundary between the evanescent and propagating regions, with the evanescent wave becoming an internal wave as it pass through the turning depth.

proximation to account for wave propagation in non-uniform stratifications in propagating regions. For multi-layered stratification profiles, internal waves have been shown to tunnel through an evanescent region of fluid and the transmission coefficient of incident internal wave energy across the evanescent region can be calculated with linear theory [4]. Further work on tunneling includes smooth changes in natural frequency and the inclusion of a shear flow [5, 6]. Gregory and Sutherland [7] found that the transmission coefficient was larger for internal waves that tunneled through a weakly stratified region instead of a well-mixed region. Mathur and Peacock [8] extended this work for transmission and reflection of internal waves and varied the scale of the transitional region. They found that a wave beam will adjust to a varying stratification and be either amplified or diminished based on the characteristics of the stratification, as long as the changes in the stratification occurred over a sufficiently large distance. Rapid changes in stratification led to wave scattering. Sutherland [9] found an analytical solution for the transmission coefficient for an arbitrary number of density staircases that are all equal in size, and also used simulations to calculate the transmission coefficient for uneven length staircases. Sutherland found, similar to the results of Ghaemsaidi et al. [10], that density staircases can act as a filter allowing only internal waves with long horizontal wavelengths and high frequencies to completely pass through the staircase region. Paoletti and Swinney [11] used exponential density profiles and stratifications to investigate internal wave reflection and transmission from a turning depth. Their results compared well with the viscous theory of Kistovich and Chashechkin [12] which allowed for arbitrary stratifications. Each of these cases assumed that internal waves were formed in a propagating region and then pass into an evanescent region, but did not investigate waves formed in an evanescent region passing into a propagating region.

Few studies have been conducted which investigate both evanescent and propagating regions. Using linear theory, Nappo [2] showed that in a two-layer, constant N fluid, with an abrupt change from an evanescent to a propagating region, propagating internal wave energy is dependent upon the strength of the stratification in the propagating region. Paoletti et al. [13] used numerical simulations validated with experiments to characterize the radiated power of internal waves generated from a turning depth with varying stratifications and compared their results to an estimated maximum tidal power. The radiated power was calculated at a fixed location near the topography while the turning depth location was varied. They found that steep-sloped topography generated waves with less power than topography with more gentle slopes. They also saw that the presence of a turning depth greatly reduced the radiated power compared to the internal waves formed in a propagating region from the same topography. Their work provides valuable insight on relative power transferred from the tides into wave motion near topography. In this work, we investigate the kinetic energy transmitted to propagating waves only. We will use experiments and a linear theory analysis to explore the effect of non-uniform stratification on wave generation in evanescent regions and focus on the resultant internal wave kinetic energy in propagating regions.

As mentioned previously, the shape of the topography from which waves are generated has an important affect on the energy content of the waves. When investigating topographically generated internal waves, topographies are frequently divided into different categories based on criticality. Criticality is defined $\epsilon = S_{top,m}/S_{wave}$ where $S_{top,m}$ is the maximum topographical slope and $S_{wave} = \sqrt{\omega^2/(N^2 - \omega^2)}$ is the slope of the generated waves (assuming no rotation). Topographies in propagating regions are considered subcritical ($\epsilon < 1$), critical ($\epsilon = 1$), or supercritical ($\epsilon > 1$). Internal wave energy has been estimated for subcritical topography for constant stratifications [14], depth varying stratifications and a finite depth ocean [15, 16]. Work has also been done for supercritical topographies both experimentally and with a viscous linear theory model [17, 18]. However, for evanescent waves, ϵ is undefined because S_{wave} is imaginary in an evanescent region. Paoletti et al. [13] used a novel technique to define an effective height of the topography, based on both the slope of the topography and the stratification profile. Using this, they could estimate radiated power for internal waves generated from evanescent waves formed from topography. They found that internal wave power is significantly decreased in the presence of a turning depth. Their results compared well with previous research on topographically generated internal waves and varying stratifications.

In this work we account for the effects of topography shape and the distance from the topography to the turning depth in realistic stratifications to investigate the influence of turning depths on the local kinetic energy of internal waves generated from evanescent regions. Specifically, experiments and a new linear model are used with an exponential N profile such that waves are generated in an evanescent region and pass into a propagating region. Average internal wave kinetic energy is quantified in the propagating region as a function of average Froude number in the evanescent region ($\overline{Fr_1} = \omega/N$) and H/D, the relative distance between the topography and the turning depth. These results represent the first ever analytical model of an evanescent wave generating an internal wave through a turning depth with varying natural frequency and the kinetic energy associated with each wave. The numerical theory is supported by experiments.

The paper is outlined as follows. Section II describes the experimental setup and analysis, and details the analytical model. Results are given in Section III, with an oceanic case study in IV. Section V concludes with a summary of the work.

II. METHODOLOGY

A. Experimental Procedures

All experiments were performed in an acrylic tank with a length, width, and height of 2.45 m, 0.15 m, and 0.91 m, respectively. To create the density profile, a modified version of the double bucket method was used [19]. Two peristaltic pumps controlled the flow rates of fresh and salt water which were joined and slowly filled the tank. Density measurements using an Anton Par density meter were taken every 2 cm before experiments began, and then

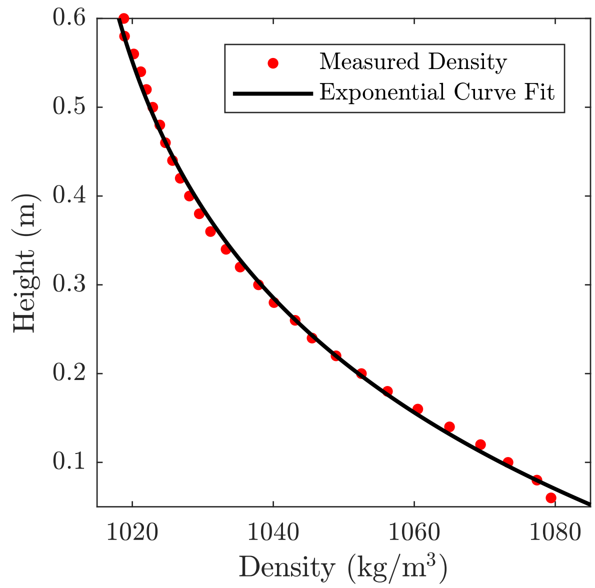

FIG. 2. The measured density is shown in red points and the exponential curve fit is the black line.

every 5 cm after every fourth experiment. Density measurements were fit to the equation

$$\rho = a\exp(bz) + c \tag{2}$$

where ρ and z have units of kg/m^3 and meters, and a (kg/m^3), b (m^{-1}), and c (kg/m^3) are coefficients calculated from the exponential fit with an average $R^2 = 0.997$ for all cases. This density profile ensures a varying N profile for every experiment, with N defined by Eq. (1) and ranging from 0.3 to 2.0 s^{-1}. In Fig. 2 the measured density and calculated exponential curve fit is shown. These data come from Case 17 shown in Table I. The density increases with decreasing height, starting at the top of the tank (z = 0.6 m) and moving down to the bottom at z=0 m.

As shown in Fig. 3, the ocean-topography system is inverted with the topography at the surface and lower values of N at the base of the topography. As z decreases, N increases. A stepper motor controls the oscillation frequency and excursion length of the topography generating waves. Matting was placed at the bottom of the tank to dampen reflections. Two Gaussian topographies were used in the experiments with curves of the form

$$h = H\exp(-x^2/B^2) \tag{3}$$

where H is the peak height of the topography and $B^2 = W^2/18$. Here, W is the width of the topography when the height of the topography has decayed to 1% of H. The first

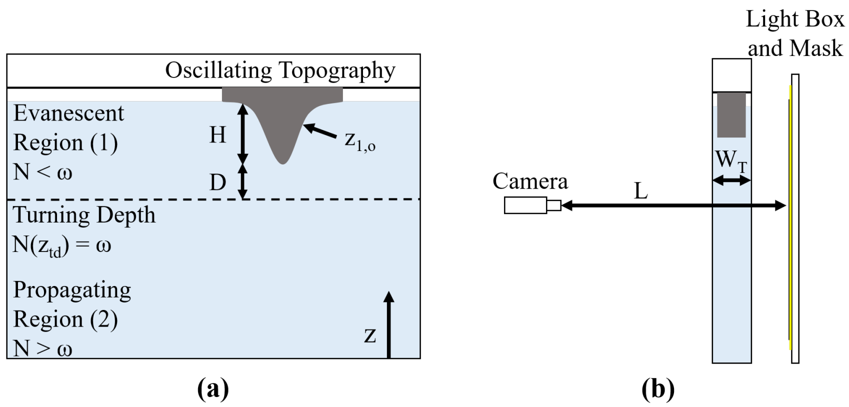

FIG. 3. Experimental tank and visualization system schematic. In (a), the front view of tank is shown with internal wave regions and turning depth as labeled. In (b), the side view of the setup with camera for synthetic schlieren imaging is shown.

topography is defined by $W/H = 1.8$ (medium topography) and the second by $W/H = 0.45$ (steep topography). $H = 10$ cm for both topographies.

Two non-dimensional numbers were used to describe each each experimental setup. First, H/D is a ratio of the height of the topography to the distance between the tip of the topography and the turning depth (D in Fig. 3a). This ratio provides a relative measure of the number of topographic heights between the source and propagating region. Values of H/D ranged from 0.311 to 2.128, where the higher values indicate the topography is closer to the turning depth. The other non-dimensional number is the average Froude number in the evanescent region which is defined as

$$\overline{Fr_1} = \omega_f / \overline{N_1} \tag{4}$$

where the subscript "1" refers to the evanescent region (see Fig. 3a) and ω_f is the forcing frequency of the topography. The Froude number is used to characterize the stratification profile in the evanescent region. Table I provides the details of each case, including the coefficients for the density profile [Eq. (2)], the height of the water in the tank, the horizontal wavenumber, the oscillation frequency of the topography, the height of the turning depth, the excursion length of the topography, and values for H/D and $\overline{Fr_1}$.

The topography was forced at an oscillation frequency ω_f. The location of the Gaussian

TABLE I. A summary of experiments and experimental parameters. Cases 1-14 used the medium topography ($W/H = 1.8$), while cases 15-24 used the steep topography ($W/H = 0.45$). Water height, z_{td}, and L are given in centimeters.

Case	a (kg/m^3)	b (m^{-1})	c (kg/m^3)	Water Height	k_d (m^{-1})	ω_f (s^{-1})	z_{td}	L	H/D	$\overline{Fr_1}$
1	100	-2.36	993	57.5	28.39	1.04	32.7	4.13	0.67	1.15
2	97.7	-2.35	994	57.3	28.26	1.00	34.9	4.23	0.81	1.14
3	95.2	-2.55	998	57.3	28.48	0.95	38.1	4.07	1.09	1.13
4	110.4	-1.35	975	67.3	28.57	0.95	35.9	3.99	0.47	1.11
5	101.6	-1.51	984	67.2	28.26	1.04	21.9	4.23	0.28	1.18
6	89.8	-2.17	999	63.4	28.29	0.85	45.3	4.21	1.23	1.10
7	84.9	-2.48	1005	63.3	28.09	0.85	42.4	4.37	0.92	1.14
8	92.6	-2.39	997	61.7	28.28	0.86	45.5	4.22	1.62	1.10
9	86.9	-2.81	1004	61.1	28.51	0.81	46.5	4.04	2.15	1.11
10	92.6	-2.39	997	57.5	28.26	0.93	38.4	4.24	1.10	1.12
11	95.2	-2.64	1003	61.7	32.29	1.21	19.8	1.46	0.31	1.30
12	95.2	-2.64	1003	61.4	31.04	1.08	28.1	2.24	0.43	1.24
13	119	-1.87	982	63.5	28.39	1.13	28.8	4.14	0.41	1.17
14	117	-1.76	981	63.3	28.15	1.00	40.3	4.32	0.77	1.10
15	88.8	-3.71	1008	69.3	67.64	1.04	29.7	4.34	0.38	1.41
16	87.8	-3.50	1007	69.3	62.85	1.24	19.3	5.05	0.28	1.50
17	87.8	-3.50	1007	60.6	63.95	1.17	22.6	4.88	0.41	1.37
18	92.2	-4.01	1011	60.5	70.96	0.96	34.1	3.90	0.71	1.29
19	94.7	-4.49	1014	61.0	57.67	0.81	41.2	5.94	1.25	1.24
20	85.1	-4.27	1014	60.9	67.38	0.86	36.9	4.38	0.85	1.28
21	89.6	-4.38	1014	60.8	65.76	0.86	37.8	4.61	0.91	1.27
22	91.8	-4.54	1014	60.5	67.57	0.77	42.7	4.35	1.62	1.22
23	91.8	-4.54	1014	60.4	67.52	1.00	31.1	4.36	0.60	1.37
24	89.8	-4.52	1015	60.2	66.03	1.00	30.6	4.57	0.59	1.37

profile in space and time is described as

$$z_{top}(x,t) = H \exp\left[\frac{-(x - L\sin\omega t)^2}{B^2}\right] \tag{5}$$

where L is the excursion length of the topography, $-0.09 \leq x \leq 0.09$ m for the medium topography, and $-0.0225 \leq x \leq 0.0225$ m for the steep topography. After 15 oscillation periods of the topography, which allowed the waves to reach steady state, images were recorded with a jAi Cv-M4+Cl progressive scan camera for three minutes at 6 fps and processed with the commercial software DigiFlow [20]. The camera shown in Fig. 3b was focused on the mask of random dots illuminated by a light box behind the tank and synthetic schlieren was used to calculate variations in density for each experiment. Digiflow calculates values of $\nabla\rho'/\rho_0$, where ρ' is the density perturbation. Using the z derivative and multiplying these values by the gravitational constant, an equation for the variation in the natural frequency between the initial undisturbed image and each subsequent image, similar to Eq. (1) is derived:

$$\Delta N^2 = \frac{-g}{\rho_0}\frac{\partial\rho'}{\partial z} \tag{6}$$

With ΔN^2, the kinetic energy of the internal waves can be estimated using the method described by Wunsch and Brandt [21]. By using the continuity equation

$$\frac{\partial u}{\partial x} + \frac{\partial w}{\partial z} = 0 \tag{7}$$

and defining

$$\frac{\partial \Delta N^2}{\partial t} = -\frac{\partial(N^2 w)}{\partial z} \tag{8}$$

the WKB approximation is used to approximate kinetic energy. Internal wave velocities and the natural frequency are defined as planar waves multiplied by slowly varying amplitudes:

$$u(x,z,t) = \int \tilde{U}\exp\left[i(kx + mz - \omega t)\right]\mathrm{d}k\mathrm{d}\omega \tag{9}$$

$$w(x,z,t) = \int \tilde{W}\exp\left[i(kx + mz - \omega t)\right]\mathrm{d}k\mathrm{d}\omega \tag{10}$$

$$\Delta N^2(x,z,t) = \int \Delta\tilde{N^2}\exp\left[i(kx + mz - \omega t)\right]\mathrm{d}k\mathrm{d}\omega \tag{11}$$

where $\tilde{U}$, $\tilde{W}$ and $\Delta\tilde{N^2}$ are Fourier amplitudes. Using Eqs. (7) and (8), where the derivatives of the amplitudes are assumed negligible, and taking a two dimensional Fourier transform along the horizontal (x) direction and through time (t), Wunsch and Brandt derive

$$KE_2 = \frac{\omega^2 N^2}{k^2(N^2 - \omega^2) + (\omega\partial_z N^2/N^2)^2}\left|\frac{\Delta\tilde{N^2}}{N^2}\right|^2 \tag{12}$$

where $KE = |\tilde{U}|^2 + |\tilde{W}|^2$, k is the horizontal wavenumber, and the subscript "2" indicates the propagating region. Unfortunately, this equation is not valid in the evanescent region because of the exponential decay of evanescent wave amplitudes and imaginary vertical wavenumber. These are accounted for by first defining

$$q^2(z) = k^2(1 - N^2(z)/\omega^2) \tag{13}$$

where $m = iq$ is the imaginary vertical wavenumber in the evanescent region [2, 3]. The velocities and natural frequency then become

$$u(x, z, t) = \int \tilde{U} \exp(qz) \exp[i(kx - \omega t)] \mathrm{d}k\mathrm{d}\omega \tag{14}$$

$$w(x, z, t) = \int \tilde{W} \exp(qz) \exp[i(kx - \omega t)] \mathrm{d}k\mathrm{d}\omega \tag{15}$$

$$\Delta N^2(x, z, t) = \int \Delta\tilde{N}^2 \exp(qz) \exp[i(kx - \omega t)] \mathrm{d}k\mathrm{d}\omega \tag{16}$$

Following the same methodology described above for Eq. (12), we find

$$KE_1 = \left| \frac{-q\omega\Delta\tilde{N}^2}{k(\partial_z N^2 + qN^2)} \right|^2 + \left| \frac{i\omega\Delta\tilde{N}^2}{\partial_z N^2 + qN^2} \right|^2 \tag{17}$$

for the evanescent region. We will denote this as KE_1 as it is the first region where waves are formed.

To use Eq. (12) and Eq. (17), the experimental data is first filtered by performing a Fourier transform in the vertical direction. The vertical wavenumber will vary throughout the experiment due to the variation in N. The Fourier coefficients corresponding to the lowest possible vertical wavenumber ($m = 0$) and above the highest expected wavenumber are zeroed. The highest expected wavenumber is defined as $m_{max}^2 = k^2(N_{max}^2/\omega^2 - 1)$. An inverse Fourier transform is then applied to the filtered data and is sorted into a timeseries of rows representing horizontal slices of the experimental data. Each row is the height of a single pixel. A 2D Fourier transform in x and t is then performed on a timeseries row to create $\Delta\tilde{N}^2$. Results are shown for Case 2 at two different locations in Fig. 4 with contours of $\Delta\tilde{N}^2$ plotted against frequency (ω) and horizontal wavenumber (k). In Fig. 4a, the horizontal slice is at z = 0.4 m, in the evanescent region, while the data in Fig. 4b is in the propagating region at z = 0.22 m. The excitation frequency for this case is $\omega_f = 1.00$. Comparing the two figures, this frequency peak is seen clearly. The expected

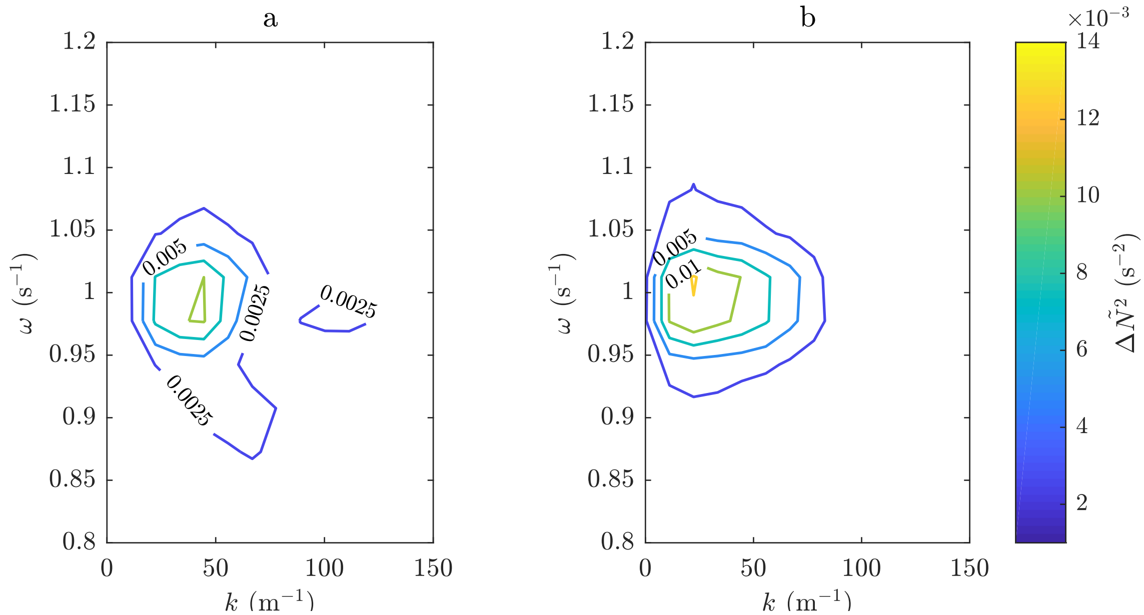

FIG. 4. Fourier amplitudes of ΔN^2 in the evanescent region (a) and propagating region (b) are shown in contours increasing by 0.0025 for each line. Both figures uses the same scaling. The highest value for the contour lines for (a) is 0.01 s^{-2} and for (b) is 0.0125 s^{-2}.

dominant horizontal wavenumber, k_d, for a specific case is found by defining the horizontal wavelength, λ_x, as the width of the topography plus the excursion length or

$$\lambda_x = W + L \tag{18}$$

Then the wavenumber for each case, $k_d = 2\pi/\lambda_x$, gives $k_d = 28.26$ m^{-1} for Fig. 4. Although the Fourier amplitudes show a peak near the expected wavenumber and excitation frequency, $\Delta\tilde{N}^2$ amplitudes do not match exactly with the expected frequency and wavelength and there is some leakage into nearby frequencies and wavenumbers. The kinetic energy is calculated at all wavenumbers and frequencies for each individual row with its corresponding N^2 and $\partial_z N^2$ values using Eq. (12) and Eq. (17). Kinetic energy data is then filtered by summing energy values for the three wavenumbers and three frequencies nearest to the expected values. This is done to allow for a comparison to the linear theory model, which uses only one wavenumber, k_d, and the forcing frequency, ω_f, while also preventing an underestimate of kinetic energy due to the $k - \omega$ spreading. Also, because of the topography and the local turbulence in its wake, the kinetic energy of the evanescent region is only calculated below the tip of the topography.

B. Theory

Using the WKB approximation, a linear, Boussinesq, 2D model was used calculate the kinetic energy that passes from the evanescent region through the turning depth and into the propagating region, accounting for the exponential natural frequency profile. Linear theory is a good approximation because $u_{top}/(\omega_f W) < 1$ for all cases [15], where u_{top} is the average velocity of the topography. The maximum value in our cases is 0.38 and the effects of this will be discussed further in Section III. The WKB approximation is valid away from the turning depth where $N^2 >> \lambda_z(\partial N^2/\partial z)$ [3]. In the following sections we will analytically calculate kinetic energy in the evanescent region and the propagating region, and then demonstrate how the two regions can be matched at the turning depth where the WKB approximation is not valid. Within each region the vertical velocity (w) is defined and the horizontal velocity (u) is found from continuity [See Eq. (7)].

With both u and w defined, the kinetic energy is defined as

$$KE = u^2 + w^2 \tag{19}$$

for comparison with experiments. Each case in Table I is reproduced with a linear theory analysis using the given experimental parameters, including the calculated λ_x and k_d from Eq. (18). No other data from the synthetic schlieren experiments are needed to initialize the theoretical analysis.

1. *Evanescent Region*

The vertical velocity in the evanescent region varies due to the variation in the N profile which affects the vertical wavelength. In the same manner as the experimental energy calculations in Section II A, the vertical wavenumber will be defined as $m = iq$, with q defined by Eq. (13). Following the work of Pedlosky [3] in a propagating region with $N = f(z)$, for the evanescent region we introduce θ_1,

$$\theta_1(z) = \int_{z_{1,0}}^{z} q dz \tag{20}$$

where the subscript "1" refers to the evanescent region. $A_{1,0}$ and $q_{1,0}$ are defined at the height $z_{1,0} = h(B)$ as shown in Fig. 3a for the medium Gaussian topography. Using q and

θ, the vertical velocity can be defined as

$$w_1(x,z,t) = A_1 \exp[i(kx - \omega t)] \exp(\theta_1) \tag{21}$$

$$A_1(z) = A_{1,0}/(q/q_{1,0})^{1/2} \tag{22}$$

Assuming a slip condition at the topography [22], the wave velocity can be calculated by using the time derivative of Eq. (5) and setting it equal to Eq. (21) such that $dz_{top}/dt = w_1(x = B, t = 0)$ [See Eq. (3)].

Using continuity [Eq. (7)], the horizontal velocity is computed as

$$u_1(x,z,t) = \frac{-w_1}{ik}\left[\frac{-dq/dz}{2q} + q\right] \tag{23}$$

The kinetic energy of the evanescent region is calculated using $KE_1 = u_1^2 + w_1^2$.

2. Propagating Region

Following the work of Pedlosky [3], velocities in the propagating region, assuming a varying natural frequency, are defined by

$$w_2(x,z,t) = A_2 \exp(i(kx - \omega t + \theta_2)) \tag{24}$$

$$u_2(x,z,t) = \frac{-w_2}{k}\left[\frac{-dm/dz}{2im} + m\right] \tag{25}$$

$$A_2(z) = A_{2,0}/(m/m_0)^{1/2} \tag{26}$$

$$\theta_2(z) = \int_{z_0}^{z} m dz \tag{27}$$

$$m^2(z) = k\left[N(z)^2/\omega^2 - 1\right] \tag{28}$$

where continuity has again been used to define u_2. Note that the subscript 2 refers to the propagating region. The kinetic energy in the propagating region is calculated by $KE_2 = u_2^2 + w_2^2$. In both the evanescent and propagating regions, the amplitude, A, of the velocities varies with height. This is due to the varying natural frequency, which causes the varying vertical wavenumber, and is necessary to conserve energy [3].

3. Airy Integral Matching

As the evanescent wave moves from the topography toward the turning depth, the WKB assumptions are violated near the turning depth because $N^2 \sim \lambda_z(\partial N^2/\partial z)$. This also causes

q to decrease to zero, creating a discontinuity at the turning depth. The Airy function can be used to patch over the discontinuity [23, 24] if the WKB approximation is extended past where it is valid [6]. This patch is used to match the vertical velocity of the evanescent wave to the propagating region. Following Lighthill [23], the vertical wave velocity with the Airy integral is

$$w_a(x, z, t) = Q_{0,w}\ \mathrm{Ai}(\beta^{1/3}z - \beta^{1/3}z_{td})\exp[i(kx - \omega t)] \tag{29}$$

where β is defined by $\beta = m^2/(z_{td} - z)$. The amplitude of $Q_{0,w}$ is found by matching Eq. (29) to Eq. (21) at $z_{1,a} = z_{td} + 0.01(2\pi/\overline{q})$, or 1% of the average vertical wavelength (λ_z) above the turning depth in the evanescent region. A range of percentages from 0.1% to 10% were compared to understand the effect of the start and end points of the Airy integral. Decreasing the percentage causes a decrease in the average kinetic energy, but the changes of kinetic energy below 1% were minimal, both for the medium and steep topographies. This percentage should be altered if there is a significant increase in the model domain and may be dependent on the vertical resolution of the model.

Continuity and w_a, Eq. (7) & Eq. (29) are used to derive the form of the horizontal velocity in the Airy integral

$$u_a(x, z, t) = Q_{0,u}\ \frac{i\beta^{1/3}}{k}\mathrm{Ai}'(\beta^{1/3}z - \beta^{1/3}z_{td})\exp[i(kx - \omega t)] \tag{30}$$

where Ai′ is the first derivative of the Airy function with respect to z.

Above the turning depth, the vertical velocities are set equal such that $w_1 = w_a$ at $z = z_{1,a}$ and $Q_{0,w}$ is solved. This procedure is repeated for the horizontal velocity with $u_1 = u_a$ at $z = z_{1,a}$ to find $Q_{0,u}$. While continuity is used to find the form of u_a, using the same amplitude as w_a defines a horizontal velocity in the Airy region that is inconsistent with the horizontal velocity in the evanescent and propagating regions. The amplitude $Q_{0,u}$ provides better consistency throughout the Airy region, but is not used in the propagating region. Instead, the wave amplitude below the turning depth, $A_{2,0}$ is calculated by setting $w_a = w_2$ at $z_{a,2} = z_{td} - 0.01(2\pi/\overline{m})$, and continuity is used to define u_2 from w_2, as defined in the previous section. It is assumed that both $Q_{0,w}$ and $Q_{0,u}$ are constant through the Airy integral region as the variation in the natural frequency is small over the small change in height.

4. Completed Model

We now explore the importance of the terms $(-dq/dz)/2q$ and $(-dm/dz)/2im$ in Eqs. (23) and (25), respectively. These higher order terms, which are not usually found in the horizontal velocity, appear because the amplitude of the velocity is a function of depth. When assuming that the amplitude, natural frequency, and vertical wavenumbers vary slowly, the variation of the vertical wavenumbers (dq/dz or dm/dz) is relatively small and can be neglected. This assumption breaks down near the turning depth, due to the rapid variation of q and m in that region, indicating they should remain in the equations for velocity. However, the use of the Airy integral to connect the evanescent and propagating regions does not include these terms. Figure 5 depicts the two different scenarios for Case 4 with height on the ordinate and kinetic energy on the abscissa. The dashed line indicates the location of the turning depth with the evanescent region above the turning depth and the propagating region below. The horizontal dash-dot line below the turning depth marks the height corresponding to a 10% increase in N relative to the excitation frequency of 0.95 s^{-1}. Kinetic energy with the higher order terms included is indicated by the solid line, while the dotted line represents kinetic energy when these terms are neglected. For both scenarios, kinetic energy begins at a maximum at the top of the figure and then decreases as the wave moves through the evanescent region. An increase in energy is seen near the turning depth, with a larger increase when the higher order terms are included. Below the turning depth, both scenarios decrease in kinetic energy through the propagating region. Away from the turning depth, the kinetic energy collapses to a single line. Each of the 24 experimental cases were compared with and without the higher order terms and the average error from the region between the end of the Airy integral and a 10% increase in N is 20%. However the majority of this error is due to the sharp increase comes from the sharp increase in amplitude at the end of the Airy integral. Neglecting this increase and again comparing the kinetic energy, the average error is 13%. We will ignore the higher order terms in this work, but it may be necessary to retain them in future work if more rapid changes in natural frequency are of interest.

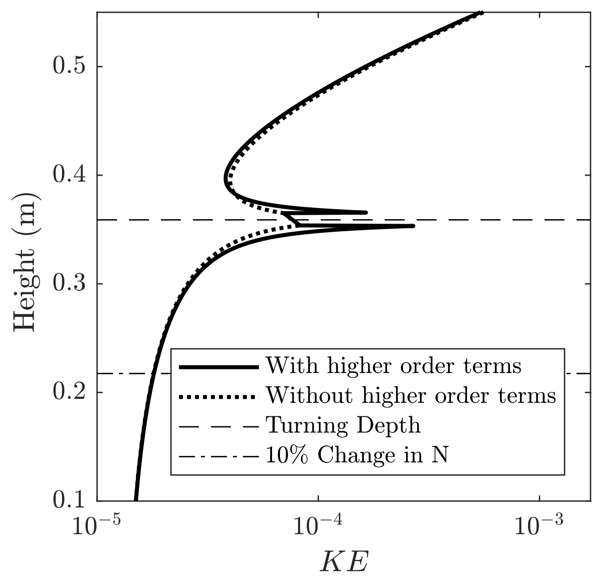

FIG. 5. The kinetic energy as a function of height is shown for the scenarios of including or excluding dq/dz and dm/dz when calculating the horizontal velocity. The turning depth is shown by the dashed horizontal line and the dash-dot line indicates the height of a 10% increase in N from the turning depth.

III. RESULTS

First, the normalized kinetic energy, KE^*, over the height of the experiment is analyzed. Figure 6 shows both the experimentally calculated and theoretically predicted KE^* over height for four cases. The ordinate is height in meters where $z = 0$ is at the bottom of the tank. The abscissa is KE^*, or KE/KE_{norm} where KE_{norm} is the average of the kinetic energy of the three pixel locations below the topography height, $z = z_{total} - H$. Because the presence of the topography generated spurious values near the topography in the experimental data, only data below the topography was analyzed. To maintain consistency between the model and the experimental analysis, the kinetic energy at the same three height locations were averaged to calculate KE_{norm} in the theoretical model as well. However, the model was averaged over only one period and one horizontal wavelength because of its periodic nature. All experimental tests were run for three minutes which provided between 21 and 35 periods for the different test cases. At least two horizontal wavelengths were captured in the field of view in the experiments for the medium topography and at least five for the steep. Figures 6a and 6b compare the model and experimental KE^* values for

Cases 1 and 8 respectively, where the medium topography was explored. Figures 6c and 6d are Cases 18 and 20, steep topography test cases. In all graphs, the solid line represents experimental data while the dotted line represents model results. The horizontal dashed line shows the location of the turning depth (z_{td}), which is determined by $N(z_{td}) = \omega_f$. Although the ordinate is the same across all four plots, the abscissa varies for each. Starting in the upper right hand corner of each plot (near the topography), normalized kinetic energy is at a maximum and as height decreases, and N increases, the normalized kinetic energy decreases exponentially as the evanescent wave travels downward and decays. At the turning depth there is a slight increase in energy due to the decrease in q as N approaches ω_f which causes an increase in the amplitudes of u and v [See Eqs. (21) and (22)]. The Airy integral is used to connect the two evanescent and propagating region. Below this, a propagating internal wave exists with relatively constant normalized kinetic energy. Within Fig. 6, there are variations in the vertical structure of the experimental energy, the model generally overestimates the kinetic energy for the medium topography, and the model significantly underestimates kinetic energy of the steep topography. Each of these results will be explored in the following paragraphs.

Differences in the vertical structure of KE^* between the model and the experiments may be partially explained by the density profile. In Fig. 2, although the curve fit used in the model follows the density measurements well, with $R^2 = 0.997$, there are some local variations in the density profile within the experimental tank that do not match exactly with the curve fit. Density values vary both slightly above and slightly below the curve fit. These local fluctuations can lead to variations in the experimental energy profile that is not reflected in the model. Also, because each of the four cases shown here have different density profiles and experimental setups, they all have different structures so an averaging scheme is introduced below. The experimental energy for Fig. 6a and b show an added decay in kinetic energy far from the turning depth. This decay is possibly due to reflected wave beams destructively interfering with the main propagating wave as it nears the bottom of the tank. For all cases, this interference was not seen near the turning depth. Because of this, the kinetic energy in the propagating region was averaged over a region below the turning depth by

$$\overline{KE_2} = \frac{1}{\Delta z_{Fr2}} \int KE \, dz \tag{31}$$

where Δz_{Fr2} is the height from the end of the Airy integral ($z_{2,a}$) to the height where the av-

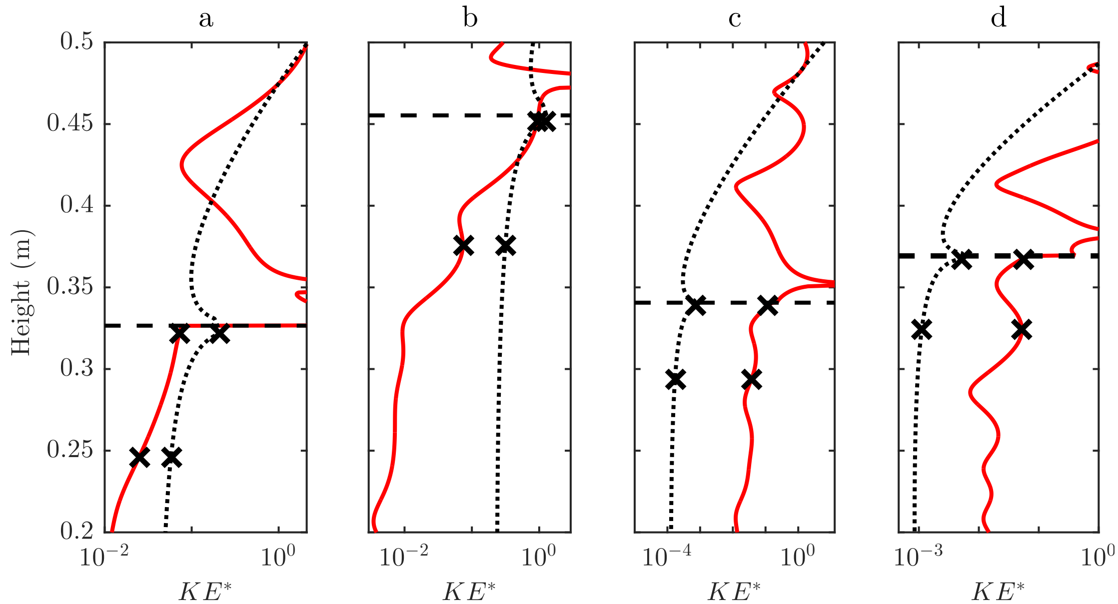

FIG. 6. Normalized kinetic energy is shown as a function of height for two cases. The solid lines are experimentally calculated KE^* while the dotted represent model results. Data from (a) and (b) come from Cases 1 and 8 which used the medium topography, while (c) and (d) are Cases 18 and 20 and used the steep topography. The turning depth location, z_{td} is marked with a dashed line. The black x markers indicate the distance over which kinetic energy is averaged in the propagating region.

erage Froude number in the propagating region is 0.952. This corresponds to a 10% increase in N from the turning depth into the propagating region. This relatively short distance is considered here to focus directly on kinetic energy transferred through the turning depth and into the propagating region. Starting and ending locations of Δz_{Fr2} are demarcated in Fig. 6 with black x's for each case. This average kinetic energy is also normalized giving $\overline{KE_2^*} = \overline{KE_2}/KE_{norm}$.

For the medium topography in Figs. 6a and 6b, the average, normalized kinetic energy of the experiment is $\overline{KE_2^*} = 0.048$ and $\overline{KE_2^*} = 0.335$, respectively. This means that approximately 5% and 34% of the kinetic energy near the topography is transferred into the propagating region. The model predicts percentage of kinetic energy transfer for these two cases to be 9% and 48%. This overestimate is most likely due to non-linearities, such as viscosity, within the experiment that are not accounted for in the model.

In the steep topography cases shown in Fig. 6c and Fig. 6d, the experiment and model follow the same qualitative trends, however the model underestimates $\overline{KE^*}$ throughout the majority of both the evanescent region and propagating region. For Fig. 6c, the model predicts $\overline{KE_2^*} = .00028$ while the experiment indicates $\overline{KE_2^*} = 0.049$. Similarly for Fig. 6d, $\overline{KE_2^*} = 0.00026$ for the model and $\overline{KE_2^*} = 0.033$ for the experiment. We explain this difference by noting the movement of the steep topography creates turbulence near the topography and turbulence generated internal waves are seen within the experiments. These turbulence generated waves have a variety of wavelengths, but also show signs of resonant triad behavior in some cases. Near the turning depth, an exchange of energy was seen between the turbulence generated waves and the topographically generated waves. For example, in Cases 15 and 16 the turbulence generated waves had a frequency of approximately half of the forcing frequency, and as the topographically generated evanescent wave passed into the propagating region, the turbulence waves lost energy while the newly formed internal waves increased in energy. Similar to Fig. 4, Fig. 7 shows the Fourier amplitudes of $\Delta\tilde{N}^2$ (scaled by a factor of 10^3) in the evanescent (a) and propagating (b) regions of Case 15. The scales for both (a) and (b) are the same, but here the frequency is normalized by the forcing frequency, ω_f, and the horizontal wavenumber is normalized by k_d from Table I. In Fig. 7a, there are peaks at $k^* = 0.15$ and 0.95, with $\omega_f^* = 0.5$. These peaks are no longer clear in Fig. 7b, but these two waves approximately sum to 1 in both frequency and wavenumber, forming a triad with the expected frequency and wavenumber, and could be feeding into the peak seen at (1,1) in Fig. 7b. Because the linear theory model does not take into account the generation or interaction of turbulence generated waves, there are steep topography cases where the model underestimates KE^*. Further investigation into the combined effect of turning depths and resonant triads could provide new information into the influence of turbulence generated waves in the ocean, but is beyond the scope of this work.

To understand the effects of topography placement relative to the turning depth (see D in Fig. 3a) on propagating internal wave energy, Fig. 8 shows $\overline{KE_2^*}$ as a function of H/D for all 24 cases. Circles represent the medium topography and triangles represent the steep topography. Filled in markers are values from experiments and open markers are calculated using the linear theory model. Normalized average kinetic energy is shown on the ordinate with a logarithmic scale, and H/D is the abscissa with a linear scale. Four trend lines have been added to the data, one for each of the four symbols. In all cases, the data show that

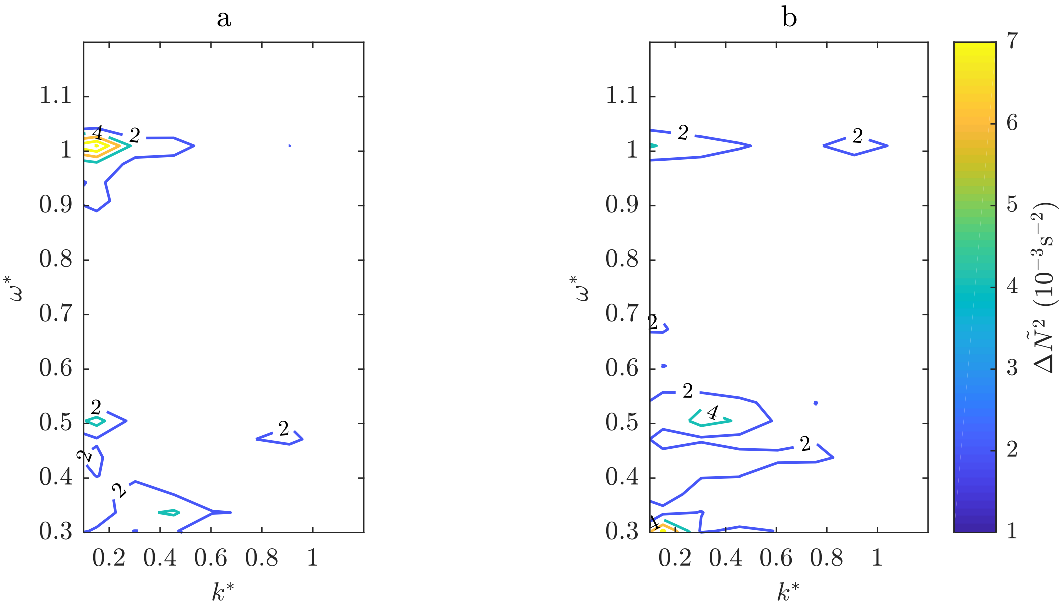

FIG. 7. Contours of $\Delta\tilde{N}^2$ for Case 15 as a function of ω^* and k^* in the evanescent (a) and propagating (b) regions. $\Delta\tilde{N}^2$ values have been scaled by a factor of 10^3.

increasing H/D, which decreases the relative distance from the topography to the turning depth, leads to an increase in kinetic energy in the propagating region. Since the evanescent wave decays over a shorter distance for high values of H/D, more kinetic energy is present at the turning depth and is subsequently transferred to the propagating region.

For the medium topography, the model trend line is similar to the experimental trend line. Each fit is defined by

$$\overline{KE_2^*} = \exp[C_1(H/D)^{C_2}] \tag{32}$$

The experimental values of C_1 and C_2 are -1.68 and -1.89 with $R^2 = 0.86$, while the model values are -1.42 and -1.40 with $R^2 = 0.98$. Here R^2 refers to the goodness of fit between the trend line and the data points, with $R^2 = 1$ indicating a perfect fit. For $H/D < 0.72$, both the model and the experiment trend lines show $\overline{KE_2^*} < 0.1$ and further decreases in H/D leads to a large decrease in kinetic energy transmitted into the propagating region. For $H/D > 0.72$, the model over estimates the normalized kinetic energy of the experiment. At $H/D = 2.2$, the experiment trend indicates that 43.5% of the initial energy from the evanescent region will pass into the propagating region, while the model predicts 62.5%. When $H/D > 0.72$, the experiment and model values match well, with the model indicating, on average, 11.9% more energy passing into the propagating region.

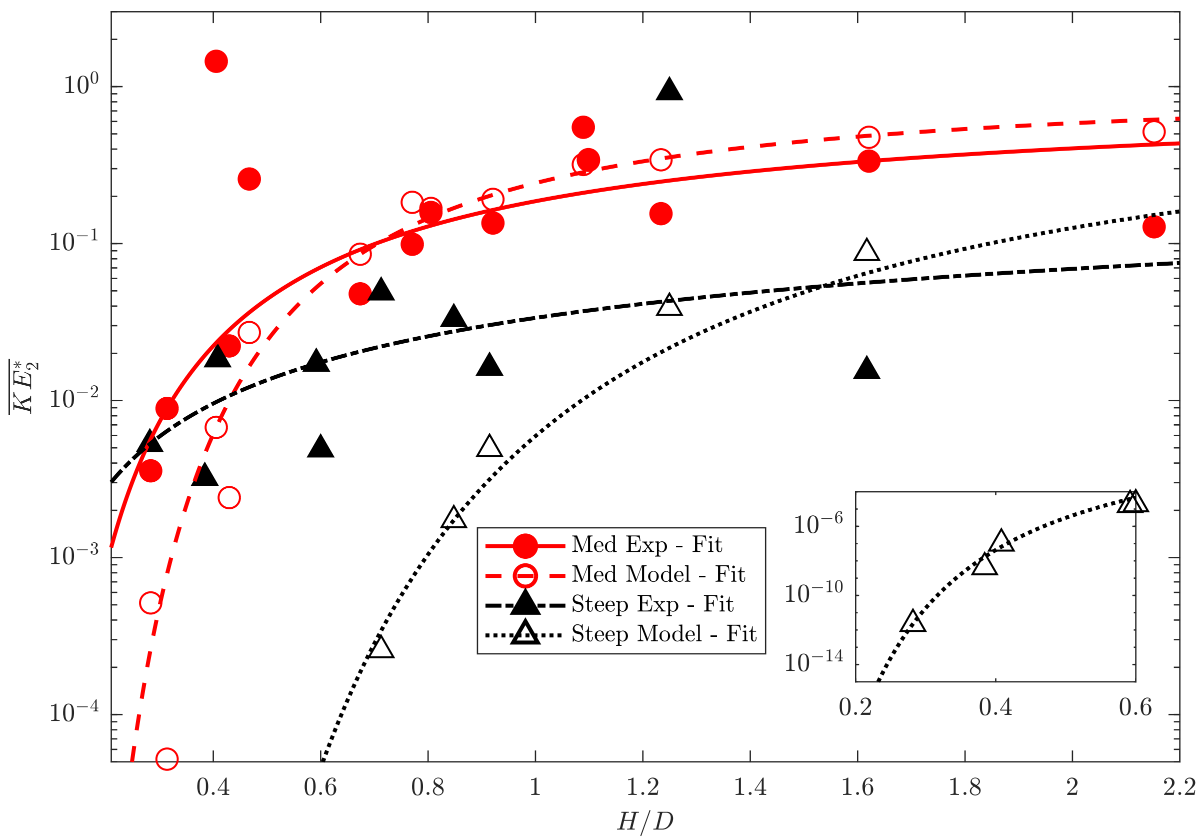

FIG. 8. The average, normalized, kinetic energy in the propagating region as a function of H/D for both the medium and steep topographies with experimental and model values. Red circles represent the medium topography, with closed filled circles representing experimental data and open for the model. Steep topography data is represented with black triangles, again with the filled triangles representing experimental data and open for the model. The inset contains five steep topography model points with normalized kinetic energy values less than 10^{-5}.

For the steep topography, the model generally underestimates the experimental values. Equation (32) was also used to fit trend lines to the data with $C_1 = -5.04$, $C_2 = -0.42$ and $R^2 = 0.53$ for the experimental data and $C_1 = -5.13$, $C_2 = -1.30$ and $R^2 = 0.99$ for the model data. As mentioned previously, some of the tests showed an interaction between the turbulence generated waves and the internal waves in the propagating region. The large difference in experimental and model values occurs for low values of H/D and for $\overline{KE_2^*} < 0.001$. It is possible that the turbulence generated waves contribute a relatively constant amount of energy to the internal wave field, and at lower values of H/D this is more significant because less topographically generated energy is present. Also, one of

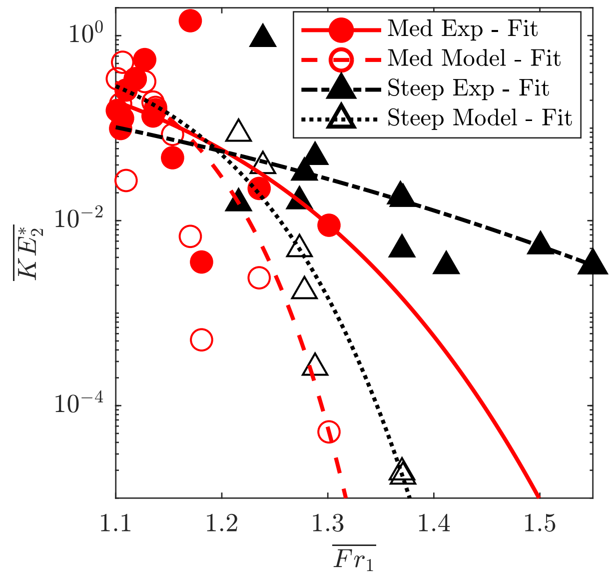

FIG. 9. $\overline{KE_2^*}$ is shown as a function of $\overline{Fr_1}$. The symbols and lines follow the same legend as shown in Fig. 8.

the requirements for using linear theory is that the $u_{top}/(\omega_f W) < 1$, meaning that the excursion length must be less than the length scale of the topography [15]. While the medium topography always met this criteria with values of $O(10^{-2})$ the steep topography had values of $O(10^{-1})$.

Figure 8 also indicates that for $H/D > 0.25$, the medium topography has a higher relative kinetic energy in the propagating region than the steep topography. Linear theory shows that without a turning depth present, a steep, narrow topography generates internal waves with higher kinetic energy than shallower, wide topography [25]; however, the presence of a turning depth introduces new dynamics. The medium topography, which has a larger wavelength, generates more kinetic energy in the propagating region than the steep topography, which has a smaller wavelength. This phenomena was seen by Paoletti et al. in their experiments and numerical models [13]. They also used a medium and steep topography with the same W/H ratios as reported here and found that in the presence of a turning depth, the medium topography has about an order of magnitude higher radiated internal wave power. We also see this trend for normalized kinetic energy for $H/D > 0.25$.

An approximation of the strength of the evanescent region can be represented by $\overline{Fr_1}$ [Eq. (4)]. As $\overline{Fr_1}$ increases, the strength or size of the evanescent region also increases. The averaged, normalized kinetic energy in the propagating region as a function of $\overline{Fr_1}$ is shown in Fig. 9. For both the medium and the steep topographies, increasing $\overline{Fr_1}$ decreases $\overline{KE_2^*}$ and at $\overline{Fr_1} > 1.2$, $\overline{KE_2^*}$ decreases rapidly. A higher value of $\overline{Fr_1}$ is indicative of a high ω_f or low N and thus a relatively weak wave as the fluid cannot sustain the motion of the evanescent wave [See Eqs. (20-23)]. $\overline{Fr_1}$ has less of an influence on normalized, propagating kinetic energy for the steep topography in the experiments than is seen for the medium topography. The greatest discrepancy between the model and the experiments for the steep topography occurs when $\overline{Fr_1} > 1.3$ and $\overline{KE_2^*} < 10^{-3}$. This discrepancy for the steep topography is likely due to the non-linear effects seen in the steep topography experimental data that are not accounted for in the model.

The curve fits follow Eq. (32), replacing H/D with $\overline{Fr_1}$. The medium topography experimental curve fit to the data ($C_1 = -0.90$, $C_2 = 6.29$, $R^2 = 0.37$) follows the general trends of the model curve fit ($C_1 = -0.35$, $C_2 = 12.72$, $R^2 = 0.94$), but with greater kinetic energy when $\overline{Fr_1} > 1.16$. The curve fits for the steep topography experiment ($C_1 = -1.76$, $C_2 = 2.68$, $R^2 = 0.36$) and model ($C_1 = -0.49$, $C_2 = 9.85$, $R^2 = 0.90$) show significant differences, but the model line follows the trend of the medium topography curves, especially for the experimental values. While not all of the cases are shown in Fig. 9, each curve was fit to the entire applicable set of data. For high $\overline{Fr_1}$, the steep topography maintains more kinetic energy in the propagating region than the medium topography. This will be explored further with the model in the following paragraphs. The medium and steep topography trend lines for the model predict a maximum $\overline{KE_2^*}$ of 0.30, meaning 30% of the original kinetic energy is retained in the propagating region. However, the experiment trend line for the medium topography indicates almost 20%, while the steep topography experiments are just over 10%.

With the experimental and model relation established, we now exercise the model further to explore a more direct relationship between the different dimensionless variables. Figure 10 shows $\overline{KE_2^*}$ as a function of both H/D (shown with different line markers) and $\overline{Fr_1}$ (abscissa). Here three different values of H/D are chosen for each topography and $\overline{Fr_1}$ is varied by changing the height of the evanescent region and the height of the topography while other variables (ω_f, W/H, and N profiles) are held constant. As seen in the previous figures, increasing H/D and decreasing $\overline{Fr_1}$ leads to an increase in relative kinetic energy. For the medium topography at $\overline{Fr_1} = 1.11$, the average kinetic energy transmitted into the propagating region increases from 6% to 78% by increasing $H/D = 1$ to $H/D = 3$. This

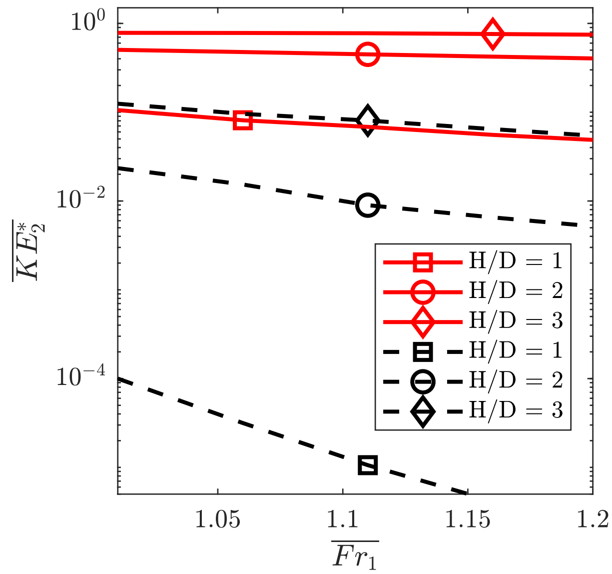

FIG. 10. $\overline{KE_2^*}$ as a function of H/D and $\overline{Fr_1}$ for the analytical model. The solid red line indicates the medium topography, while the dashed black line is the steep topography. Markers for H/D as shown.

increase is larger for the steep topography under the same condition and $\overline{KE_2^*}$ increases from less than 0.001% to 8%. The model also shows that with a high H/D for the steep topography and low H/D for the medium topography, the steep topography can transmit greater kinetic energy to the propagating region than the medium topography for the same $\overline{Fr_1}$. This was seen in Fig. 8 where some cases of the steep topography had higher kinetic energy than the medium topography, but only when the steep topography has a higher H/D value.

Figure 11 depicts scenarios for varying topographic slope and stratification profiles. In Fig. 11a, $\overline{KE_2^*}$ increases with increasing W/H, which represents the relative slope of the topography. The width of the topography was varied while maintaining a constant height of 10 cm, which also varied the horizontal wavelength according to Eq. (18). The Gaussian parameter B [Eq. (3)] was varied based on W. Parameters for the density profile were held constant and follow Case 4 from Table I. The excursion length and excitation frequency were also maintained as values from Case 4. With $W/H = 10$, almost 80% of the kinetic energy from the evanescent region is transmitted into the propagating region. For Case 4, with $W/H = 1.8$, marked on Fig. 11a as a red circle, only 2.5% of the initial kinetic energy passes into the propagating region. As shown previously, in the presence of a turning depth, topography with steep slopes generate internal waves with less kinetic energy in the propagating region for a given H/D or $\overline{Fr}$. Also W, the width of the topography, indicates an increase in the wavelength of the topography. A topography with a larger wavelength will generate evanescent waves with higher kinetic energy which will then pass into the propagating region.

In Fig. 11b and 11c, the influence of the exponential stratification is explored. With a density profile of $\rho = a\exp(bz)+c$, the stratification is defined as $N^2 = -gab\exp(bz)/\rho_0$. For both Fig. 11b and 11c, H/D, ω_f, W/H, L, and $\overline{Fr_1}$ are held constant and match Case 4. The topography height varies to maintain H/D, and width is defined by $W = 1.8H$, maintaining the same W/H ratio as the medium topography. In Fig. 11b, a is normalized by the reference density ρ_0. Increasing a/ρ_o from 0.092 to 0.149 causes a 95% decrease in the normalized, average kinetic energy in the propagating region. Although a weaker stratification leads to initially more energetic evanescent waves, the stratification also increases more rapidly throughout the evanescent region with a larger value of a, causing an overall decrease in the kinetic energy in the propagating region. However, as shown in Fig. 11c, increasing bH causes an overall increase in the kinetic energy in the propagating region. Here, b is normalized by H, the height of the topography. Increasing bH causes an initially weaker stratification but a larger b, meaning a value that is less negative, causes the stratification to increase at a slower rate. Thus the evanescent wave does not decay as rapidly and more kinetic energy passes through the evanescent region into the turning depth. Although bH changes by less than one order of magnitude, $\overline{KE^*}$ increases by three orders of magnitude.

IV. OCEAN CASE STUDY

We now use the linear model to investigate the propagating internal wave kinetic energy generated by an oceanic feature. To use the linear model we estimate the shape of the topography, the natural frequency profile, and the velocity of the tide and assume a frame of reference where the topography moves through quiescent water. Feature data comes from the *Ocean Data View 4* using a GEBCO 2014 6' worldwide bathymetry map [26]. The feature is at 15° N, ranges from 129.6° to 130.2° E, and can be approximated as a Gaussian topography as seen in Fig. 12. In the figure, the data from the GEBCO bathymetry map is shaded and the Gaussian curve fit laid over the feature of interest with a dashed line. For

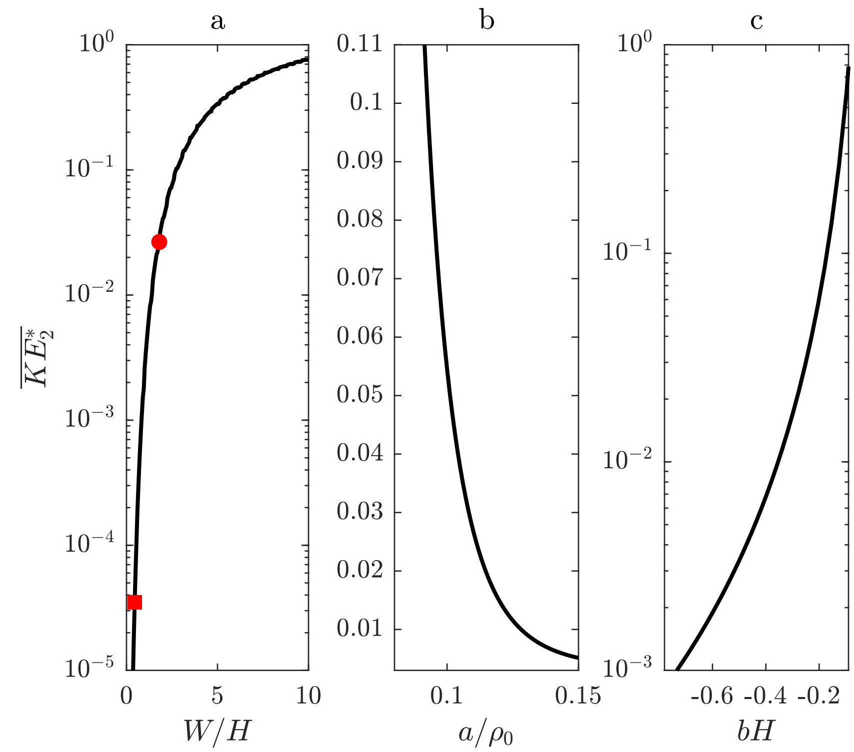

FIG. 11. $\overline{KE_2^*}$ is shown as a function of W/H, a/ρ_o, and bH, showing the effects of topographic shape (a) and an exponential density profile in (b) and (c). In (a), the square and circle indicate $W/H = 0.45$ and 1.8, or the steep and medium topographies, respectively.

use in the linear theory model, the Gaussian curve fit is centered at zero. The equation for the fit is given by

$$z_{top,ocean} = 5868 - 831.3 \exp\left(\frac{-x^2}{10970^2}\right) \tag{33}$$

with $-20000 < x < 20000$ m and the base of the feature at a depth of 5868 m. In order to apply the feature to the model, it is assumed that the feature is two dimensional. We assume a tidal velocity of 4 cm/s for the M2 semidiurnal tide based on the work by Poulain and Centurioni [27], who also indicate that in the Philippine Sea the M2 tide oscillates zonally, or left to right over the topography shown in Fig. 12.

Using data from the World Ocean Circulation Experiment (WOCE) for cruise P08N located at 129.99° E, 15.01° N, the natural frequency profile was calculated. This location is the closest data near the chosen oceanic topography [28]. We followed the method of King et al. [1] to smooth and average the CTD data. Temperature and salinity data is averaged over a set depth or bin size and then the natural frequency is calculated with the Gibbs Sea

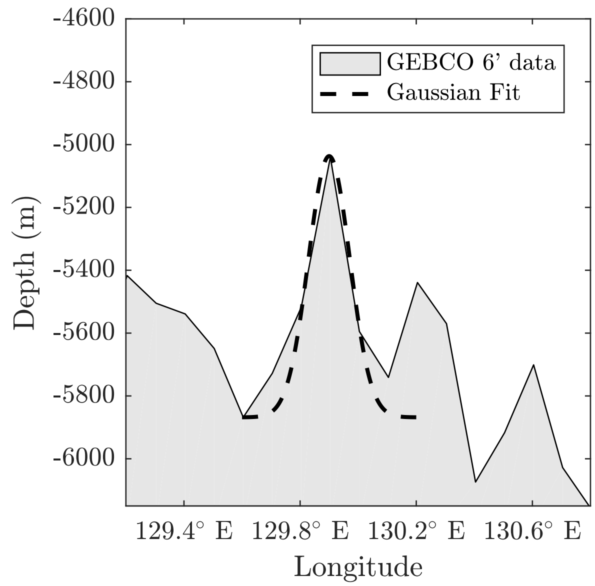

FIG. 12. Data from the GEBCO worldwide bathymetry map is indicated by the shaded portion, with a Gaussian curve fit through topographical feature analyzed in this work.

Water TEOS-10 Matlab tool box [29]. King et al. recommend a bin size of between 100 and 200 m and we chose 200 m for this data set because it provided a smooth curve while retaining the major characteristics of the profile. The natural frequency profile indicates a turning depth at a height of 4367 m, which is above the topography. However, the profile does not extend down to the bottom of the oceanic feature. A curve fit was applied to the smoothed data to extend the profile to the bottom of the topography. The curve fit is given by

$$\ln(N^2) = a_1 \exp\left[\frac{-(z-b_1)^2}{c_1}\right] + a_2 \exp\left[\frac{-(z-b_2)^2}{c_2}\right] \tag{34}$$

where $a_1 = -15.14$, $b_1 = 4831$, $c_1 = 6553$, $a_2 = -5.788 \times 10^{12}$, $b_2 = 3.658 \times 10^4$, and $c_2 = 5993$ and ln refers to the natural logarithm. The natural frequency profile is plotted in Fig. 13a. To maintain consistency between this figure and those given previously, the evanescent region is at the top of the figure with the propagating region beginning at 4367 m.

Based on the oceanic feature and natural frequency profile, we use the analytical model to calculate a kinetic energy profile shown in Fig. 13b. Kinetic energy is again normalized by the evanescent wave energy at the tip of the topography to be consistent with the previous results. Starting at the top left corner, KE^* decreases rapidly through the evanescent

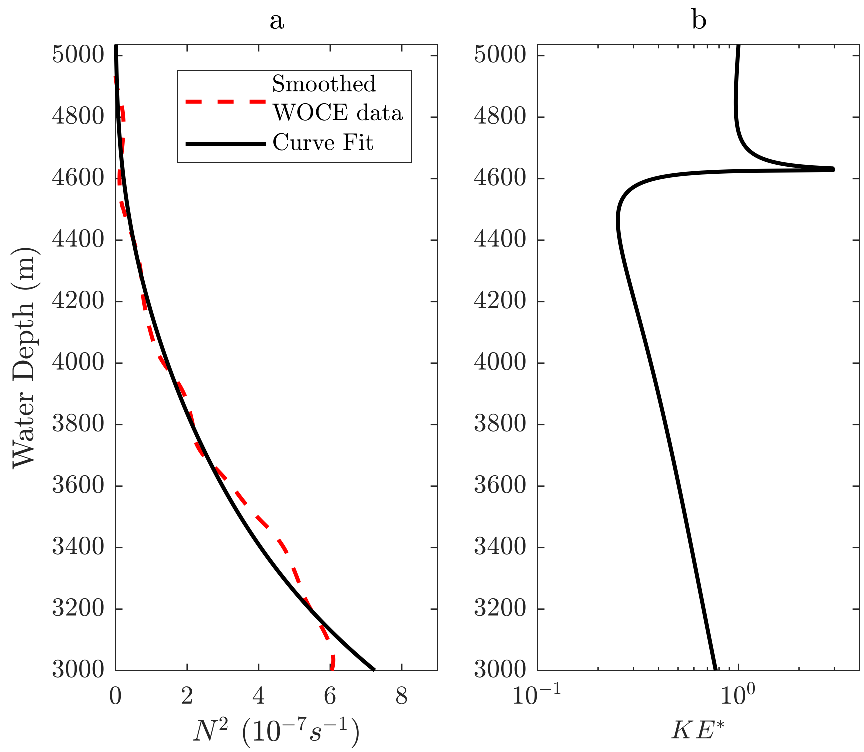

FIG. 13. WOCE data is used to calculate N^2 indicated by the red dashed line in (a), while the black line is the curve fit of the data used for the model analysis. The normalized kinetic energy calculated from the model is shown in (b) as a function of depth.

region until it reaches the turning depth. The Airy integral provides the needed patch into the propagating region, where the kinetic energy of the internal wave at first decreases and then increases. In the experimental cases, shown previously, this increase was not seen due to the limited depths of the propagating region. Kinetic energy increases due to increasing N which causes an increase in m as well. Although the velocity amplitudes are inversely proportional to $m^{1/2}$, kinetic energy is proportional to A^2 and m^2, leading to an overall increase in energy. However, the energy flux, $c_{gz}\{E\} = -\rho_0 A^2 m\omega/(2k^2)$, is constant throughout the propagating region [3].

The Airy integral in Fig. 13b uses a smaller percentage of the vertical wavelength than the experiments. Testing the model with the experiments indicated that using 1% of the vertical wavelength to start and end the Airy integral minimized the effects of the matching condition (See Section II B 3). For this oceanic scenario, this percentage is reduced to 0.001%. Increasing or decreasing this value led to an increase in the overall kinetic energy in the propagating region. The minimum value was chosen to prevent an overestimate of the kinetic energy.

The average, normalized kinetic energy from the end of the Airy region to $\overline{Fr_2} = 0.952$ at a depth of 4587 m is $\overline{KE_2^*} = 0.57$. The minimum KE^* in the propagating region occurs near the turning depth at a depth of 4466 m with a value of 0.25. This 25% transmission could be taken as the energy that is able to pass through the turning depth and into the propagating region, and is a nontrivial portion of the original kinetic energy of the evanescent wave. While this model is a linear approximation of a non-linear event, it does indicate that internal waves generated from evanescent waves passing through the turning depth can still maintain a significant portion of the original kinetic energy formed from M2 tidal oscillations across oceanic bathymetry within evanescent regions.

V. CONCLUSION

Past investigations of the influence of evanescent regions on internal waves have focused on an internal wave approaching an evanescent region and the subsequent reflection and/or transmission of internal wave energy at the turning depth. Here, we studied the scenario where evanescent waves approach a turning depth and become propagating internal waves. We expanded upon the work of Paoletti et al [13] by creating an analytical model which predicts the kinetic energy of internal waves generated from an evanescent region. The model is then compared to experiments and the effects of topographical shape, stratification profile ($\overline{Fr_1}$), and the relative distance between the topography and the propagating region (H/D) on internal wave kinetic energy were explored.

Similar to Paoletti et al [13], we found that the medium Gaussian topography, with a more gentle slope, has a higher kinetic energy in the propagating region than the steep Gaussian topography. For high H/D and low $\overline{Fr_1}$, the medium topography theory showed that the evanescent waves transmit up to 62.5% of the kinetic energy at the topography surface into internal waves in the propagating region, while the experiments indicated a maximum of 43.5% (See Fig. 8). While not an exact match, the model predicts similar values to the experiment. However, the model does not match well with the steep topography as it approaches the limit of criticality. The experiments for the steep topography indicate the maximum kinetic energy in the propagating region is near 10% of the original kinetic energy at the tip of the topography, while the model indicates closer to 20% (See Fig. 9). As seen in Fig. 11, decreasing the slope, indicated by an increasing W/H, increases the percentage of energy transmitted into the propagating region. Also, Fig. 10 indicates that only with larger values of H/D does steep topography generate internal waves with higher kinetic energy than medium topography.

The experiments and model also indicate the importance of the stratification in estimating internal wave kinetic energy. Increasing $\overline{Fr_1}$, indicating a large, or strong, evanescent region, causes a decrease in propagating region kinetic energy. For the exponential density profile, the model indicates that low values of a/ρ and high values of bH increase $\overline{KE_2^*}$ due to a slow increase in the natural frequency in the evanescent region, causing a slower decay of the evanescent waves and more kinetic energy transferred into the propagating region.

To show a potential use of this analytical model, an oceanic case study was also explored and results show the average kinetic energy that passed from the evanescent region, through the turning depth and into the propagating region had 25% of the original kinetic energy of the evanescent wave. While this is only one case, it indicates that evanescent waves that become internal waves could transfer significant energy from tidal motions away from the topography and into the general ocean.

Future work with this model could include applying it to more oceanic topographies which are situated in evanescent regions (relative to the M2 tidal frequency) to provide an overall estimate of the kinetic energy of internal waves generated from tidal motions across topography. Also, continued investigations into the turbulence generated waves could provide insight in how to improve the model, possibly by including viscosity. As both topography shape and stratification profile impact the overall kinetic energy, this work could also be expanded upon by exploring more complex topographies and other realistic stratification profiles.

ACKNOWLEDGMENTS

This work has been supported by the Utah NASA Space Grant Consortium and by NSF Grant CBET-1606040.

---

[1] B. King, M. Stone, H. P. Zhang, T. Gerkema, M. Marder, R. B. Scott, and H. L. Swinney, "Buoyancy frequency profiles and internal semidiurnal tide turning depths in the oceans," Journal of Geophysical Research: Oceans **117** (2012), 10.1029/2011JC007681.

[2] C. J. Nappo, *An introduction to atmospheric gravity waves* (Academic Press, San Diego, California, 2002).

[3] J. Pedlosky, *Waves in the Ocean and Atmosphere* (Springer-Verlag Berlin Heidelberg, Germany, 2003).

[4] B. R. Sutherland and K. Yewchuk, "Internal wave tunnelling," Journal of Fluid Mechanics **511**, 125–134 (2004).

[5] G. L. Brown and B. R. Sutherland, "Internal wave tunneling through nonuniformly stratified shear flow," Atmosphere-Ocean **45**, 47–56 (2007).

[6] J. T. Nault and B. R. Sutherland, "Internal wave transmission in nonuniform flows," Physics of Fluids (1994-present) **19**, 016601 (2007).

[7] K. D. Gregory and B. R. Sutherland, "Transmission and reflection of internal wave beams," Physics of Fluids **22**, 106601 (2010), http://dx.doi.org/10.1063/1.3486613.

[8] M. Mathur and T. Peacock, "Internal wave beam propagation in non-uniform stratifications," Journal of Fluid Mechanics **639**, 133152 (2009).

[9] B. R. Sutherland, "Internal wave transmission through a thermohaline staircase," Phys. Rev. Fluids **1**, 013701 (2016).

[10] S. J. Ghaemsaidi, H. V. Dosser, L. Rainville, and T. Peacock, "The impact of multiple layering on internal wave transmission," Journal of Fluid Mechanics **789**, 617629 (2016).

[11] M. S. Paoletti and H. L. Swinney, "Propagating and evanescent internal waves in a deep ocean model," Journal of Fluid Mechanics **706**, 571–583 (2012).

[12] Yu. V. Kistovich and Yu. D. Chashechkin, "Linear theory of the propagation of internal wave beams in an arbitrarily stratified liquid," Journal of Applied Mechanics and Technical Physics

39, 729–737 (1998).

[13] M. S. Paoletti, M. Drake, and H. L. Swinney, “Internal tide generation in nonuniformly stratified deep oceans,” Journal of Geophysical Research: Oceans **119**, 1943–1956 (2014).

[14] T. H. Bell, “Topographically generated internal waves in the open ocean,” Journal of Geophysical Research **80**, 320–327 (1975).

[15] S. G. Llewellyn-Smith and W. R. Young, “Conversion of the barotropic tide,” Journal of Physical Oceanography **32**, 1554–1566 (2002), http://dx.doi.org/10.1175/1520-0485(2002)032<1554:COTBT>2.0.CO;2.

[16] S. Khatiwala, “Generation of internal tides in an ocean of finite depth: analytical and numerical calculations,” Deep Sea Research Part I: Oceanographic Research Papers **50**, 3 – 21 (2003).

[17] H. P. Zhang, B. King, and H. L. Swinney, “Experimental study of internal gravity waves generated by supercritical topography.” Physics of Fluids **19**, 096602 (2007).

[18] D. G. Hurley and G. Keady, “The generation of internal waves by vibrating elliptic cylinders. part 2. approximate viscous solution,” Journal of Fluid Mechanics **351**, 119138 (1997).

[19] D. F. Hill, “General density gradients in general domains: the two-tank method revisited,” Experiments in Fluids **32**, 434–440 (2002).

[20] S. B. Dalziel, G. O. Hughes, and B. R. Sutherland, “Whole-field density measurements by ‘synthetic schlieren’,” Experiments in Fluids **28**, 322–335 (2000).

[21] S. Wunsch and A. Brandt, “Laboratory experiments on internal wave interactions with a pycnocline,” Expts. in Fluids **53**, 1663–1679 (2012).

[22] T. Peacock, P. Echeverri, and N. J. Balmforth, “An Experimental Investigation of Internal Tide Generation by Two-Dimensional Topography,” Journal of Physical Oceanography **38**, 235 (2008).

[23] J. Lighthill, *Waves in fluids* (Cambridge University Press, 1978).

[24] D. Broutman, “On internal wave caustics,” Journal of Physical Oceanography **16**, 1625–1635 (1986).

[25] C. Garrett and E. Kunze, “Internal tide generation in the deep ocean,” Annual Review of Fluid Mechanics **39**, 57 – 87 (2007).

[26] R. Schlitzer, “Ocean data view 4,” (2017).

[27] P. M. Poulain and L. Centurioni, “Direct measurements of world ocean tidal currents with

surface drifters," Journal of Geophysical Research Oceans **120**, 6986–7003 (2015).

[28] S. Diggs, J. Kappa, D. Kinkade, and J. Swift, "WHP CD-ROM Version 3.0." (2002).

[29] IOC, SCOR, and IAPSO, *The international thermodynamic equation of seawater-2010: Calculation and use of thermodynamic properties.*, Intergovernmental Oceanographic Commission, manuals and guides no. 56 ed. (2010).